CHALMERS
UNIVERSITY OF TECHNOLOGY

An Enhanced Equivalent Circuit Model of Vanadium Redox Flow Battery Energy Storage Systems Considering Thermal Effects

Citation for the original published paper (version of record):
Xiong, B., Yang, Y., Tang, J. et al (2019). An Enhanced Equivalent Circuit Model of Vanadium Redox Flow Battery Energy Storage Systems
Considering Thermal Effects. IEEE Access, 7: 162297-162308.
http://dx.doi.org/10.1109/ACCESS.2019.2952212

(article starts on next page)

IEEE Access
Multidisciplinary | Rapid Review | Open Access Journal

Received September 25, 2019, accepted November 1, 2019, date of publication November 7, 2019,
date of current version November 18, 2019.

Digital Object Identifier 10.1109/ACCESS.2019.2952212

An Enhanced Equivalent Circuit Model of Vanadium Redox Flow Battery Energy Storage Systems Considering Thermal Effects

BINYU XIONG[1], (Member, IEEE), YESEN YANG[1], JINRUI TANG[1], (Member, IEEE), YANG LI[1], (Member, IEEE), ZHONGBAO WEI[2], YIXIN SU[1], (Member, IEEE), AND QINGYONG ZHANG[1]

[1]School of Automation, Wuhan University of Technology, Wuhan 430072, China
[2]National Engineering Laboratory for Electric Vehicles, School of Mechanical Engineering, Beijing Institute of Technology, Beijing 100081, China

Corresponding author: Yang Li (yang.li@whut.edu.cn)

This work was supported in part by the Natural Science Foundation of China under Grant 61703318, in part by the Major Projects of Technical Innovation in Hubei Province under Grant 2018AAA050, in part by the Open Fund of Operation and Control Renewable Energy and Storage System of National Key Laboratory under Grant DGB51201801584, and in part by the Innovation Project of Wuhan University of Technology under Grant 2019-ZDH-B1-05.

ABSTRACT Thermal issue is one of the major concerns for safe, reliable, and efficient operation of the vanadium redox flow battery (VRB) energy storage systems. During the design of the operational strategy for a grid-connected VRB system, a suitable mathematical model is needed to predict the dynamic behaviors under various operating conditions. However, conventional VRB models usually neglect the impact of temperature variations on system performance. This work develops an enhanced VRB model with the consideration of the coupling effects between the electrochemical and the thermal behaviors. The proposed model consists of two equivalent circuits. First, the electrochemical behaviors of the VRB are modeled by a second-order RC network taking account of the effects of concentration variation of the vanadium ions and the electrochemical activation. Second, a third-order Cauer network is used to model the heat transfer process in the VRB system, and the dynamic thermal behaviors of stacks, pipes and heat exchangers are characterized. Well-designed experiments and particle swarm optimization algorithm are use to identify the parametric values of the developed model. The proposed modeling method was validated experimentally using a 5kW/3kWh VRB platform, and the results show that the model is capable of accurately predicting the VRB performance under variable temperature conditions. The developed coupled electro-thermal model is then used for simulating and analyzing the performance of a VRB system operated in conjunction with a wind power plant under real-world conditions.

INDEX TERMS Vanadium redox flow battery, coupled electro-thermal model, Cauer network, thermal model, battery energy storage systems.

I. INTRODUCTION

The vanadium redox flow battery (VRB) has successfully demonstrated its competence in large-scale energy storage applications such as to provide peak shaving and power smoothing of renewable generation owning to its merits of safe operation, long cycling life, no cross contamination and flexible power/capacity design, etc. [1]–[6]. Thermal issue has been considered to be one of the major concerns for efficient and reliable operation of the VRB systems. High temperature can cause severe problems such as electrolyte precipitation and flow channel blockage which can accelerate the aging of the battery. For large-scale VRB systems, the overall roundtrip energy conversion efficiency can reach up to 80%, while the remaining 20% of the stored energy is wasted in the form of heat during the normal operation [4], [7]. The large amount of the generated heat can lead to a significant temperature rise in the electrolyte and elsewhere. This can affect the overall performance of the battery, especially after long-term operation [8]–[10]. The thermal impact due to

The associate editor coordinating the review of this manuscript and approving it for publication was Gaetano Zizzo.

shunt current and pump power loss has been investigated in [9], [11]–[13], where equivalent thermal networks have been used to describe the heat transfer process of the VRB systems. A thermal model based on energy conservation law was developed in [9] where heat generation was analyzed by incorporating the hydraulic behavior. Xing *et al.* [11] set up an equivalent thermal model using cascaded networks to describe the shunt current loss which is the unique phenomenon for flow batteries. Wei *et al.* [12] compared different stack flow patterns and analyzed the heat generation due to pump power loss. Agar *et al.* [13] investigated the heat generation and capacity fading by altering the charge/discharge currents. These studies demonstrate various approaches for thermal modeling and operation strategies.

To study the external electrical behaviors of the VRBs, equivalent circuit models have been widely used [14]–[20]. Riccardo *et al.* [14] presented a semi-empirical model considering the consumption of the auxiliary power and the operational behavior for the residential applications. However, this model only exhibits the steady-state characteristics while the dynamic behavior of the VRB is not described. Qiu *et al.* [15] proposed a reduced-order model of the VRB and the parasitic losses of the pump power was included for microgrid applications, and the model was validated using field experimental data. Tang *et al.* [16] established a dynamic model to predict the capacity loss caused by ion diffusion and side reactions occurred in the electrodes, and the relevant mechanisms can be considered in the design of the VRB control system to achieve long-term optimal operation. Furthermore, a comprehensive dynamic equivalent circuit model consisting of a voltage source, parasitic shunt bypass circuits, and a first-order resistance-capacitance network was proposed for grid analysis [21]. The model can accurately predict the dynamic process of the VRB.

However, the existing VRB models used in the above-mentioned works often neglect the coupling effect between the electrical and thermal models on the overall system performance, and thus they may fail to accurately predict the system performance when the VRB is working under highly varying operating conditions, e.g. in renewable applications. The coupled effects between the electrical and the thermal behaviors of the VRB system are presented in FIGURE 1. It can be seen from FIGURE 1 that the temperature variation may affect the electrochemical properties of the material, and it can result in concentration overpotential and ohmic loss. Meanwhile, the internal losses induced by the ohmic resistance and the concentration overpotential can also generate a large amount of heat, resulting in electrolyte temperature rise. Hence, a proper mathematical model needs to be developed to accurately predict the performance of the VRB system under various dynamic operating conditions.

In this paper, an enhanced equivalent circuit model considering the thermal effects is proposed for operational planning and real-time control of the VRB systems. The remainder of the work is organized as follows: an enhanced equivalent circuit model consisting of an electrical network and a thermal network is developed in Section II. The particle swarm optimization (PSO) method is used to identify the model parameters in Section III. In Section IV, the proposed model was validated experimentally using a 5kW/3kWh VRB platform set up in the lab. In Section V, a case study for the estimation of the temperature and voltage variation during one day is investigated in a practical scenario where the VRB is operating in conjunction with a wind power plant. The main findings are concluded in Section VI.

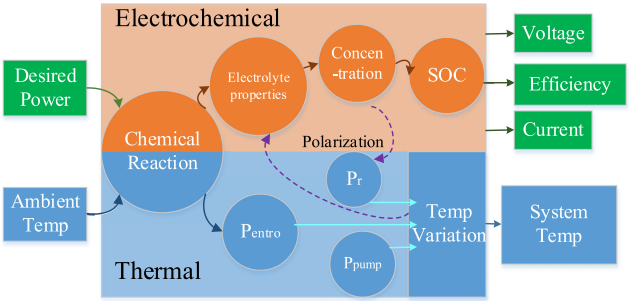

FIGURE 1. The coupled effects between the electrochemical and the thermal systems of the VRB.

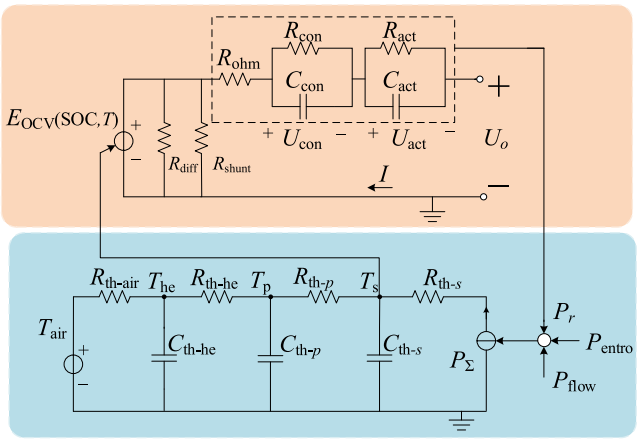

FIGURE 2. The schematic diagram of the proposed coupled electro-thermal model of the VRB system.

II. AN ENHANCED EQUIVALENT CIRCUIT MODEL

In this section, an enhanced VRB model that consists of an equivalent electrical circuit network and an equivalent thermal circuit network is proposed. The schematic diagram of the proposed coupled electro-thermal model is shown in FIGURE 2. The equivalent electrical network analogizes the electrochemical behaviors of the VRB during the charging and discharging processes, while the thermal sub-circuit describes the heat transfer process.

A. ELECTRICAL CIRCUIT MODEL

As shown in FIGURE 2, E_{OCV} represents the open-circuit voltage (OCV) of the VRB. Theoretically, OCV is determined

by the concentrations of different vanadium species, and this relationship is governed by Nernst equation, i.e. [22]

$$E_{\mathrm{OCV}} = E^{\Theta} + m\frac{RT_s}{zF}\ln\left(\frac{c_{\mathrm{V}^{2+}}c_{\mathrm{V}^{5+}}c_{\mathrm{H}^{+}}^{2}}{c_{\mathrm{V}^{3+}}c_{\mathrm{V}^{4+}}}\right) \tag{1a}$$

where $c_{\mathrm{V}^{i+}}$ $(i = 2, 3, 4, 5)$ and $c_{\mathrm{H}^{+}}$ denote the concentrations of corresponding vanadium species and the protons, respectively. Here E^{Θ} is the formal potential of the battery, R is the universal gas constant, F is the Faraday constant, z is the number of electrons transferred in the reaction, and T_s is the temperature of the electrolyte in the stack, or the stake temperature. m is the cell number in the stack. The state of charge (SOC) of the VRB can be defined as,

$$\mathrm{SOC} = \frac{c_{\mathrm{V}^{2+}}}{c_{\mathrm{V}^{2+}} + c_{\mathrm{V}^{3+}}} = \frac{c_{\mathrm{V}^{5+}}}{c_{\mathrm{V}^{4+}} + c_{\mathrm{V}^{5+}}} \tag{1b}$$

However, the concentration of the protons in a VRB is difficult to estimate, and it is commonly assumed that $c_{\mathrm{H}^{+}} = 1$ in practice [22]. With this assumption and substituting (1b) into (1a), we obtain

$$E_{\mathrm{OCV}} = E^{\Theta} + m\frac{2RT_s}{zF}\ln\left(\frac{\mathrm{SOC}}{1-\mathrm{SOC}}\right) \tag{2}$$

However, the actual OCV usually deviates from that calculated from (2) due to the omission of the proton concentration. To address the problem, (2) is modified to

$$E_{\mathrm{OCV}} = E^{\Theta} + m\frac{2RT_s}{zF}\left[k_1\ln(\mathrm{SOC}) - k_2\ln(1-\mathrm{SOC})\right] \tag{3}$$

where k_1 and k_2 are two correction coefficients. Equation (3) shows that E_{OCV} can be expressed as a function of the SOC and the stack temperature T_s, as indicated in FIGURE 2, while k_1, k_2, and E^{Θ} are three parameters that shall be identified to approximate the true OCV curve.

The relationship between the derivative of SOC and the applied current I is,

$$\dot{\mathrm{SOC}} = \frac{\eta}{C_n}(-I) \tag{4}$$

where C_n is the battery capacity and η is the instantaneous Coulomb efficiency. Note that in this paper, the applied current I is defined as positive when the battery is during discharging.

Next, based on the electrochemical principles of the VRB, a second-order RC circuit is selected in this work to analogize the fast electrochemical behaviors of the VRB [21]. As shown in FIGURE 2, the second-order RC network in the upper dashed block consists of three parts which represent three fast physiochemical phenomena inside the battery, i.e.

1) R_{ohm} is used to represent the effect of the total ohmic loss due to the resistance of the electrodes, electrolyte, membrane, etc;

2) R_{con} and C_{con} are used to model the overpotential U_{con} caused by the large concentration gradient between the bulk electrolyte and the electrode surface at the end of the charge/discharge process, i.e.

$$\dot{U}_{\mathrm{con}} = -\frac{U_{\mathrm{con}}}{R_{\mathrm{con}}C_{\mathrm{con}}} + \frac{I}{C_{\mathrm{con}}} \tag{5}$$

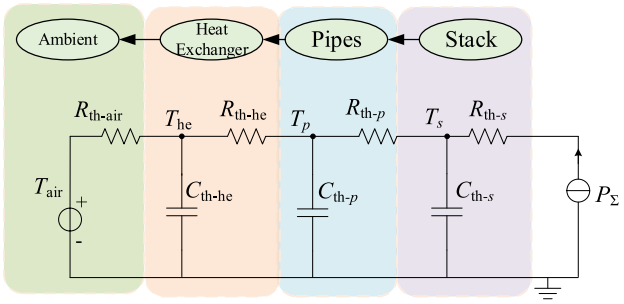

FIGURE 3. Schematic of the proposed third-order Cauer network.

3) R_{act} and C_{act} are associated with the overpotential for overcoming the activation energy of the electrochemical reactions, i.e.

$$\dot{U}_{\mathrm{act}} = -\frac{U_{\mathrm{act}}}{C_{\mathrm{act}}R_{\mathrm{act}}} + \frac{I}{C_{\mathrm{act}}} \tag{6}$$

Furthermore, the slow self-discharge phenomenon can also be observed in the VRB, which is caused by various degradation mechanisms. Two of the major mechanisms are considered in the proposed model, and both of which are represented using a resistor connected in parallel to E_{OCV}. First, R_{diff} is used to describe the unexpected diffusion of the vanadium ions across the membrane of the VRB. Second, R_{shunt} is used to describe the moving of the vanadium species through the conducting manifold and the guide channels. The total self-discharge effect can be modeled as [21],

$$R_{\text{self-dch}} = R_{\mathrm{diff}}||R_{\mathrm{shunt}} = \sum\frac{1}{\sigma}\frac{l}{S} \tag{7}$$

where S denotes the cross-sectional area of the electrode, l is the effective length, and σ is the electrolyte conductivity. With (7), the Coulomb efficiency η in (4) can be calculated by,

$$\eta = \begin{cases} 1 - \dfrac{E_{\mathrm{OCV}}}{R_{\text{self-dch}}I}, & I \neq 0 \\ 1, & I = 0 \end{cases} \tag{8}$$

From (8), it can be seen that the instantaneous Coulomb efficiency $\eta < 1$ during charging process and $\eta > 1$ during discharging process, as the consequence of the self-discharge phenomenon.

Finally, the terminal voltage U_o of the VRB can be calculated as,

$$U_o = E_{\mathrm{OCV}} - U_{\mathrm{con}} - U_{\mathrm{act}} - R_{\mathrm{ohm}}I \tag{9}$$

B. THERMAL EQUIVALENT NETWORK

As shown in FIGURE 3, the thermal sub-model is set up using a third-order Cauer network to mimic the overall heat transfer process from the stack to the ambient, via the pipes and the heat exchangers. Mathematically,

$$C_{\mathrm{th}-s}\frac{dT_s}{dt} = -\frac{1}{R_{\mathrm{th}-p}}T_s + \frac{1}{R_{\mathrm{th}-p}}T_p + P_\Sigma \tag{10}$$

$$C_{\text{th}-p}\frac{dT_p}{dt} = \frac{1}{R_{\text{th}-p}}T_s - (\frac{1}{R_{\text{th}-\text{he}}} + \frac{1}{R_{\text{th}-p}})T_p + \frac{1}{R_{\text{th-he}}}T_{\text{he}} \tag{11}$$

$$C_{\text{th-he}}\frac{dT_{\text{he}}}{dt} = \frac{1}{R_{\text{th-he}}}T_p - (\frac{1}{R_{\text{th-he}}} + \frac{1}{R_{\text{th-air}}})T_{\text{he}} + \frac{1}{R_{\text{th-air}}}T_{\text{air}} \tag{12}$$

where the subscripts s, p, he, air, represent the stack, the pipes, the heat exchangers, and the ambient, respectively, while the symbols T, R_{th} and C_{th} represent the temperature, the thermal resistance and the thermal capacitance of corresponding components, respectively.

In (13), P_Σ is the total dissipated power which causes the electrolyte temperature rise. It consists of four components, i.e.

$$P_\Sigma = P_r + P_{\text{flow}} + P_{\text{entro}} + P_{\text{self-dch}} \tag{13}$$

P_r is the power generated due to overpotential,

$$P_r = I^2\left(R_{\text{ohm}} + R_{\text{act}} + R_{\text{con}}\right) \tag{14}$$

P_{flow} is the hydraulic friction loss due to the viscosity of the electrolyte. P_{flow} is calculated by [23],

$$\begin{cases} P_{\text{flow}} = \dfrac{\Delta p_{\text{total}} Q}{\alpha} \\ \Delta p_{\text{total}} = \dfrac{\mu l Q}{\kappa S} \end{cases} \tag{15}$$

where Δp_{total} denotes the total pressure drop in the hydraulic pipes, Q is the flow rate of the electrolyte, μ is the viscosity of the electrolyte, α is the pump power efficiency, and κ is the permeability of the porous electrode.

P_{entro} is the heat released due to electrochemical reaction, and it is obtained by [22],

$$\begin{aligned} P_{\text{entro}} &= m\frac{IT_s}{zF}\left[\Delta S_r^{\ominus} + R\ln\left(\frac{c_{\text{V}^{2+}} c_{\text{V}^{5+}} c_{\text{H}^+}^2}{c_{\text{V}^{3+}} c_{\text{V}^{4+}}}\right)\right] \\ &= m\frac{IT_s}{zF}\left\{\Delta S_r^{\ominus} + 2R\left[k_1\ln(\text{SOC}) - k_2\ln(1-\text{SOC})\right]\right\} \end{aligned} \tag{16}$$

where $\Delta S_r^{\ominus}$ is the molar reaction entropy under standard conditions.

$P_{\text{self}-\text{dch}}$ is the self-discharge power and shunt current loss,

$$P_{\text{self-dch}} = E_{\text{OCV}}^2 / R_{\text{self-dch}} \tag{17}$$

C. STATE-SPACE REPRESENTATION

At this point, an enhanced equivalent circuit model (3)-(17) of the VRB has been developed to describe the coupled electro-thermal relationship. The model can be summarized in a compact continuous-time state-space form, i.e.

$$\begin{cases} \dot{\mathbf{x}} = \mathbf{A}\mathbf{x} + \mathbf{B}\mathbf{u} \\ \mathbf{y} = h(\mathbf{x}) \end{cases} \tag{18}$$

where the system matrix $\mathbf{A}$ and the input matrix $\mathbf{B}$ are given in Appendix. The state vector $\mathbf{x}$ and the input vector $\mathbf{u}$ are,

$$\begin{aligned} \mathbf{x} &= \begin{bmatrix} U_{\text{act}} & U_{\text{con}} & \text{SOC} & T_s & T_p & T_{\text{he}} \end{bmatrix}^T \\ \mathbf{u} &= \begin{bmatrix} I & P_\Sigma & T_{\text{air}} \end{bmatrix}^T \end{aligned}$$

The stack temperature T_s and the terminal voltage U_o are considered as two measurable output variables of the model, i.e.

$$\begin{aligned} \mathbf{y} &= \begin{bmatrix} T_s \\ U_o \end{bmatrix} \\ &= \begin{bmatrix} x_4 \\ \left(E^{\ominus} + m\frac{2Rx_4}{zF}\left[k_1\ln(x_3) + k_2\ln(1-x_3)\right]\right) \\ -x_1 - x_2 - R_{\text{ohm}}u_1 \end{bmatrix} \end{aligned}$$

where x_i $(i = 1-6)$ represents the i-th element of $\mathbf{x}$.

III. MODEL PARAMETER IDENTIFICATION METHOD

In this section, the method to determine the parameters of the developed VRB model (18) is proposed and described.

First, a self-discharge test is designed and carried out to identify the self-discharge resistance $R_{\text{self}-\text{dch}}$ as described in (7). In this test, the VRB is first fully charged and then relaxed under no load condition for a long period of time. The self-discharge time $T_{\text{self}-\text{dch}}$ and the battery capacity C_n are recorded until SOC dropped to 0%. With the nominal battery voltage U_n, the self-discharge resistance can thus be calculated as

$$R_{\text{self-dch}} = R_{\text{diff}} || R_{\text{shunt}} = U_n T_{\text{self-dch}} / C_n \tag{19}$$

Next, with the known constants R, z and F, the parameters $E^{\ominus}$, k_1 and k_2 in (3) can be determined by fitting the measured OCV-SOC curve using the least square method. Very low C rate is applied to obtain accurate OCV-SOC curve, under which condition, the temperature rise is negligible, and thus the stack temperature T_s can also be considered as a known constant. In this work, the thermal parameters in (10)−(12) and the pump parameters in (15) are assumed known as they can be obtained from literature where the VRB system shares a similar design.

The remaining parameters that need to be identified are the RC parameters R_{ohm}, R_{con}, C_{con}, R_{act} and C_{act} in the electrical equivalent circuit of the developed VRB model. In order to identify these five parameters, an optimization problem is formulated and solved by particle swarm optimization (PSO). PSO is a computationally-efficient, fast convergent, and easily-implementable evolutionary computing technique that has been widely used to optimize various mathematical problems [24]. In the algorithm, a swarm of particles (sets of parameters) move around in the search area based on the positions and velocities of the particles [25]. In the present investigation, the optimization objective is to minimize of the M-point sum of square error ε between the simulated terminal voltage $U_{o,k}$ using the proposed model and the terminal

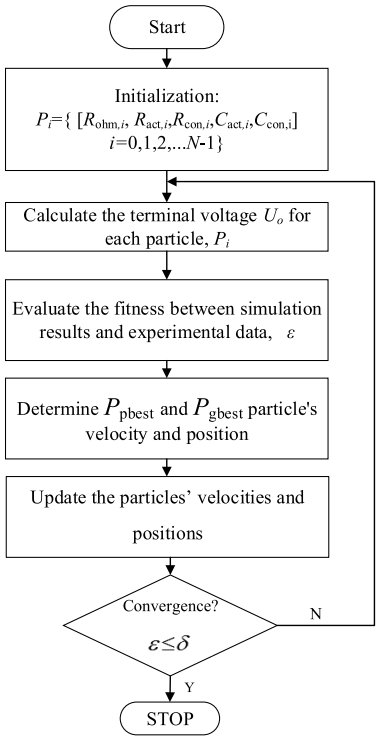

FIGURE 4. Workflow of the parameter identification method based on PSO algorithm.

voltage $\hat{U}_{o,k}$ measured from the experiment, i.e.

$$\min(\varepsilon) = \min\left(\sum_{k=0}^{M-1}(U_{o,k} - \hat{U}_{o,k})^2\right) \tag{20}$$

subject to the system model (18) and

$$\begin{aligned} R_{ohm} &\in [R_{ohm,min}, R_{ohm,max}], \\ R_{act} &\in [R_{act,min}, R_{act,max}], \\ R_{con} &\in [R_{con,min}, R_{con,max}], \\ C_{act} &\in [C_{act,min}, C_{act,max}], \\ C_{con} &\in [C_{con,min}, C_{con,max}] \end{aligned}$$

The experimental data are obtained from a single round trip charge/discharge current test. The variation of the stack temperature is relatively small compared to the large heat capacity of bulk electrolyte during the short experimental period. Thus, the stack temperature is considered constant and not included in the objective function.

The workflow of the proposed parameter identification method using PSO algorithm is shown in FIGURE 4, and the details are described as below.

Step 1: Initialize a population of N particles. The initial population of the swarm group is randomly generated conformed by uniform distribution. The position of the i^{th} particle is assigned as,

$$P_i = \text{rand}\{R_{ohm,i} \quad R_{act,i} \quad R_{con,i} \quad C_{act,i} \quad C_{con,i}\} \tag{21}$$

Step 2: Evaluate the fitness of each particle by (20);

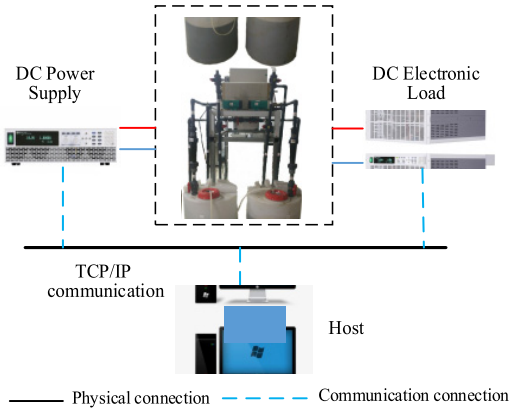

FIGURE 5. Schematic of the VRB experimental platform.

Step 3: Determine the personal best position, P_{pbest}, to obtain the minimal error,

$$P_{i,pbest} = \arg\min\{\varepsilon(P_{k,pbest}),\ k = 0, 1, \cdots, i\} \tag{22}$$

Similarly, the global best position, P_{gbest}, is determined by,

$$P_{i,gbest} = \arg\min\{\varepsilon(P_{k,pbest}),\ k = 0, 1, \cdot\cdot, i\} \tag{23}$$

Step 4: Calculate the particles' velocities, v_i, and positions, P_i, by applying the following equations, respectively,

$$v_i = \omega v_{i-1} + c_1 r_1 (P_{i,gbest} - P_i) + c_2 r_2 (P_{i,pbest} - P_i) \tag{24}$$

$$P_i = P_{i-1} + v_i \tag{25}$$

where ω denotes the inertia weight. c_1 and c_2 are learning factors. r_1 and r_2 are random numbers within (0,1].

Step 5: Step 2 to *Step 4* are repeated until fitness meets the convergence criterion. When ε reaches the minimal error δ between the measured voltage, the global solution of particle $P_{i,gbest}$ is obtained.

IV. EXPERIMENTAL AND SIMULATION RESULTS

A. EXPERIMENTAL PLATFORM

In order to identify the model parameters and validate the proposed model, a 5kW/3kWh VRB testing platform set up in authors' laboratory was used. The stack is manufactured by Golden Energy Century Company, Ltd. in China. As shown in FIGURE 5, the platform consists of a programmable DC power supply (ITECH 6533C), a programmable DC electronic load (ITECH 8818) and a host computer. The host computer sends commands to the power source and the load to control the operation of the VRB. To facilitate the instrument control, a user-defined interface was developed by VISA API in LabVIEW and installed on the host computer. The interface allows the VRB to operate in different charge/discharge modes, such as constant current (CC), constant voltage (CV), and constant power (CP) modes.

The stack of the VRB consists of 37 series-connected cells ($m = 37$) with a nominal charge/discharge current of 100 A. The specification of the testing VRB system is given in Table 1.

TABLE 1. Specification of the testing VRB system.

Configuration	Dimension
Power rating	5kW
Capacity	3kWh
Number of cells	37
Stack dimension	750mm×480mm×300mm
Concentration of vanadium ion	1.5 mol/L
Electrolyte volume	200 L
Voltage limits	40V(Low) 60V(High)
Nominal voltage	50V

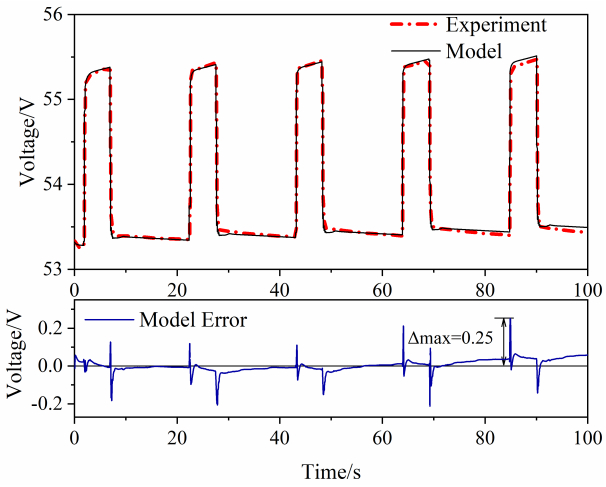

FIGURE 6. Model parameter identification under pulse charging current at SOC = 0.4.

B. PARAMETER IDENTIFICATION AND VALIDATION OF THE ELECTRICAL SUB-MODEL

Following the parameter identification procedure presented in Section III, the self-discharge test was first carried out to identify the self-discharge resistance. The total discharge time $T_{\text{self-dch}}$ is 105.5 hours, and the discharge capacity C_n is 63.8 Ah. With the nominal voltage $U_n = 50$ V, the self-discharge resistance $R_{\text{self-dch}}$ can be calculated as 82.7 Ω according to (19). Next, the parameters k_1, k_2, and E^{Θ} in (3) are 1.0, 1.1, and 52.28 V based on an experimentally-determined OCV-SOC curve using a 1/12 C constant discharge current. Furthermore, $R = 8.314$ J/(K · mol), $z = 1$ and $F = 96485$ C/mol.

The next step is to identify the five RC parameters R_{ohm}, R_{con}, C_{con}, R_{act} and C_{act} using the PSO method described in Section III. First, the reference voltage profile $\hat{U}_{o,k}$ in (20) needs to be obtained experimentally. A pulse current charging test was thus carried out at SOC = 0.4. The amplitude of the charging current was set to 10 A and the charging time is 5 s, followed by a resting period of 15 s. The measured voltage response is plotted in FIGURE 6 as the experiment results with a sampling time of 1 ms. Note that the thermal model does not need to be taken into consideration since the stack temperature T_s in this test is nearly constant. This is due to a short charging time and a negligible amount of heat.

TABLE 2. Parameter sets of PSO.

PSO Parameters	Description	T_1	T_2	T_3	T_4	T_5
N	Particle number	25	50	100	25	50
ω	Inertia weight	1	1	1	0.5	1
c_1	Learning factor	2	2	2	2	1
c_2	Learning factor	2	2	2	2	1

TABLE 3. Parameter identification results by using PSO.

Parameters	T_1	T_2	T_3	T_4	T_5
R_{ohm} (Ω)	0.064	0.051	0.043	0.052	0.051
R_{con} (Ω)	0.0042	0.0054	0.0065	0.011	0.0041
R_{act} (Ω)	0.0089	0.0041	0.0089	0.0051	0.0035
C_{con} (F)	1042.5	1563.3	2709.3	2643.8	1917.1
C_{act} (F)	4856.03	4300.6	2909.3	5572.5	5040.2
RMSE (V)	0.036	0.047	0.042	0.053	0.046
CPU Time (s)	27.81	56.04	129.18	25.23	50.24

Meanwhile, five different sets of PSO parameters, denote $T_1 - T_5$, were used to initialize the algorithm, which are listed in Table 2.

The particle number and learning factors are selected empirically according to [25], [26]. The values of the self-learning factor c_1, the social learning factor c_2 are set between 1 and 2, respectively. The upper and the lower bounds of the parameters are selected based on the estimation of the overall resistance and capacitance. In this paper, R_{ohm} is within 0.03 Ω to 0.08 Ω, R_{con} and R_{act} are within 0.001 Ω to 0.03 Ω, while C_{con} and C_{act} are within 10 F to 8000 F. The initial values of the parameters are randomly selected. The allowable tolerance ε is set to 5×10^{-5}. By applying the PSO algorithm described in Section III, the five circuit parameters were obtained and the results are given in Table 3, where it can be seen that R_{ohm} is much larger than R_{con} and R_{act}.

From Table 3, it can also be seen that the CPU time required to identify the parameters increases almost linearly as the particle number increases. Based on the results, the parameter set T_1 is selected as the identified parameters, since it has the least root-mean-square error (RMSE) with low computational time. The modeled voltage response based on T_1 is compared with the experimental results in FIGURE 6, where the sampling time of the measured voltage is 1 ms. It is observed that the voltage reproduced using the proposed model and identified parameters fits the experimental data well: the RMSE is only 0.036 V, while the maximum absolute error (MAE) is 0.25 V.

To validate the developed model and the identified parameters, three constant current charge/discharge tests were carried out for round trip cycling at the ambient temperature of 20 °C. The current magnitudes of the tests are 60 A, 80 A, and 100 A, respectively, The VRB was charged from the empty state (SOC = 0) until it had reached an upper voltage limit of 60 V. It was then discharged to a lower voltage limit around 40 V. In these tests, the terminal voltage was measured

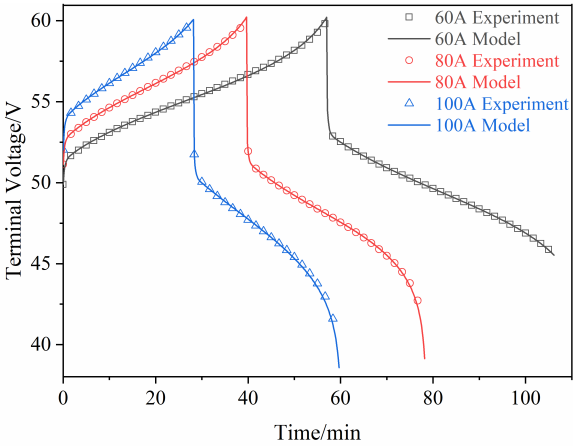

FIGURE 7. Model validation under various constant currents.

TABLE 4. Parameters of the thermal model.

$R_{\text{th-s}}$ (Ω)	$R_{\text{th-p}}$ (Ω)	$R_{\text{th-he}}$ (Ω)	$R_{\text{th-air}}$ (Ω)	$C_{\text{th-s}}$ (F)	$C_{\text{th-p}}$ (F)	$C_{\text{th-he}}$ (F)
2.1×10^{-4}	1×10^{-3}	3.8×10^{-3}	8.4×10^{-3}	4761	5.2×10^{4}	4.7×10^{5}

with the sampling time of 10 s. The same current profiles were applied to the proposed VRB model in the simulation, to obtain the terminal voltage with the identified parameters T_1 given in Table 3. Again, the stack electrolyte temperature T_s is assumed to be constant since the operation time is very short, and the self-discharge resistance $R_{\text{self-dch}}$ can also be ignored for the same reason. The experimental and simulation results are depicted and compared in FIGURE 7. As can be seen from FIGURE 7, the experimental results match the modeled curves well, and it validates that the developed model is capable of accurately predicting the dynamic behaviors of the VRB.

C. SIMULATION OF TEMPERATURE EFFECT

In order to study the temperature effect on system performance, in this section the electrolyte temperature variations of the stack, the pipes, and the heat exchanger are analyzed under several operating conditions. In this case, a constant charging/discharging currents of 60 A was applied for VRB operation. Using the identified parameters T_1, and according to (14)−(17), we have $P_r = 223.128$ W, $P_{\text{self}} = 30.01$ W, $P_{\text{flow}} = 78.5$ W, and $P_{\text{entro}} = -64.33$ W during charging and 68.91 W during discharging. According to (13), the total heat generation is therefore,

$$P_\Sigma = \begin{cases} 402.048\text{W}, & \text{during discharging} \\ 267.308\text{W}, & \text{during charging} \end{cases}$$

The heat is then transferred from the stack to the tanks via the hydraulic pipes and the heat exchanger by the electrolyte. The thermal resistances and thermal capacitances in the Cauer network are obtained using a similar technique from [12] and given in Table 4.

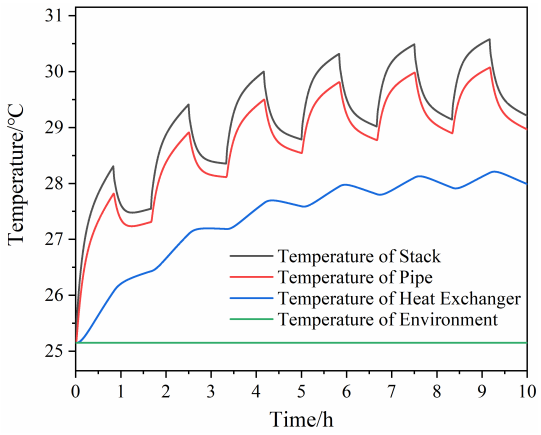

FIGURE 8. Temperature variation under constant current operation mode.

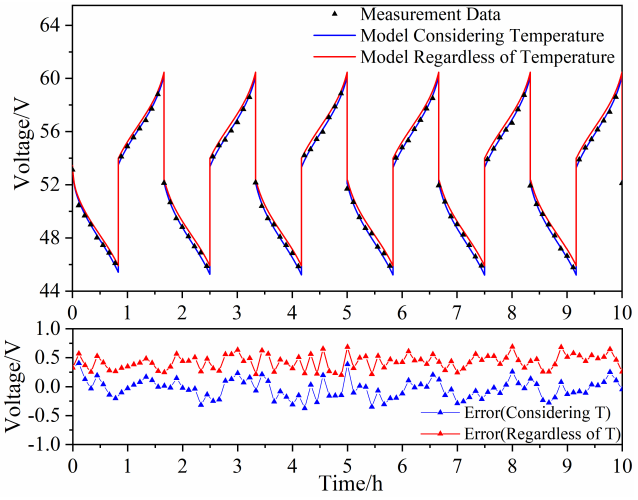

FIGURE 9. Comparison between the stack voltages considering and regardless of temperature effects.

The dynamic thermal behavior was simulated in MATLAB/Simulink R2016a. The ambient temperature T_{air} was set to 25.2 °C. The VRB was cycled by charging for 50 minutes and then discharging for 50 minutes. The simulated temperatures of the heat exchanger, the pipes, and the stack under this constant current operation are plotted in FIGURE 8. It can be seen that the stack electrolyte temperature rises by 4.5 °C, and the result is comparable to that reported in [8], where the stack electrolyte temperature rises about 5°C under a 30-A constant current test.

According to the results shown in FIGURE 8, it can be observed that the temperature rise of the electrolyte in the stack is generally higher than that in the pipes and in the heat exchanger. For example, the temperature rise of the stack electrolyte temperature is 4.3 °C after six consecutive round trip cycles, and the corresponding value is 2.7 °C for the heat exchanger. The average temperature rise of the electrolyte in the stack is 2.2 °C higher than that in the heat exchanger.

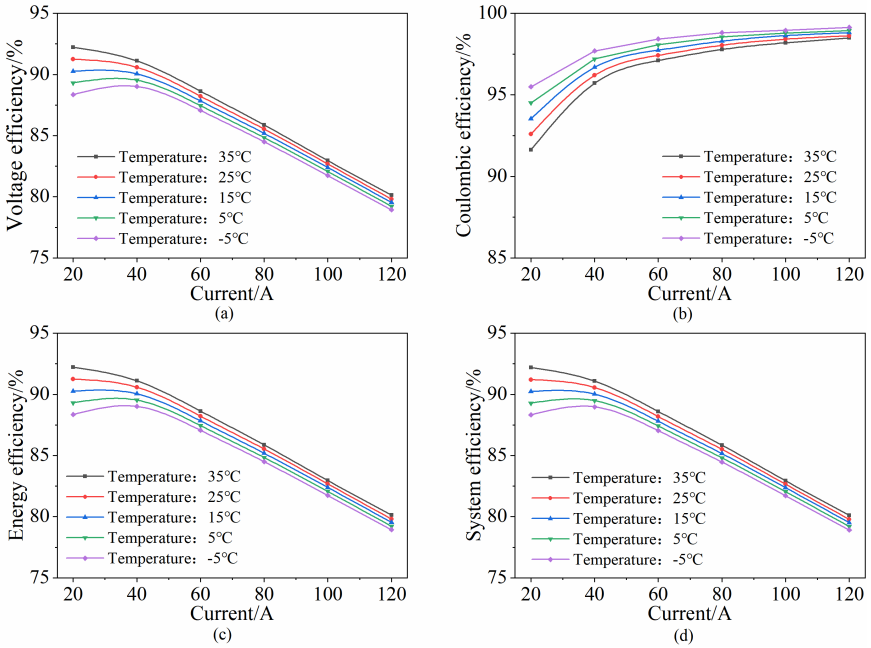

FIGURE 10. VRB efficiencies under various temperatures. (a) Voltage efficiency. (b) Coulomb efficiency. (c) Energy efficiency. (d) System efficiency.

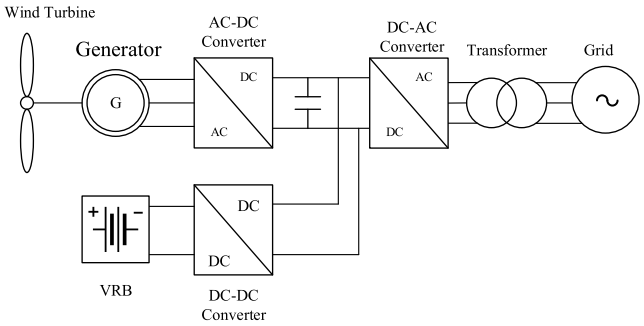

FIGURE 11. Schematic of the wind power plant-VRB hybrid system.

This is reasonable as the heat exchanger is able to dissipate more generated heat than the stack.

D. ELECTRO-THERMAL CHARACTERISTICS

In this sub-section, the proposed thermal model is validated experimentally. The experiment was carried out for six consecutive cycles with a constant charge/discharge current of 60 A, similar to that in the previous sub-section. The measured voltage was recorded and then compared with the models which with and without consideration of the temperature effect in FIGURE 9.

As the electrolyte temperature gradually increases during the charging and discharging process, the terminal voltage tends to decrease by about 0.268 V per cycle due to relatively low activation energy of chemical reactions, leading to a decrease of activation overpotential. It is easy to observe that the terminal stack voltage by the proposed coupled electro-thermal model fits well with the measured voltage, and the RMSE between the two curves is 0.171 V. In comparison, the RMSE is 0.445 V if the temperature effect is ignored. Hence, the RMSE has been reduced by 62% using our proposed model.

Next, the battery efficiencies under various temperatures ranging from −5°C to 35 °C are investigated. The simulation was carried out based on the proposed model under constant currents from 20 A to 120 A. The VRB operates from SOC = 0.1 to 0.9 for one round trip cycle. The terminal voltage, current, and capacity are measured. Commonly used battery efficiencies are defined as,

$$\text{Voltage efficiency, } VE = \frac{\int_0^{Td} U_d dt}{\int_0^{Tc} U_c dt} \tag{26}$$

$$\text{Coulomb efficiency, } CE = \frac{\int_0^{Td} I_d dt}{\int_0^{Tc} I_c dt} \tag{27}$$

$$\text{Energy efficiency, } EE = \frac{\int_0^{Td} U_d I_d dt}{\int_0^{Tc} U_c I_c dt} \tag{28}$$

$$\text{System efficiency, } SE = \frac{\int_0^{Td} \left(U_d I_d - P_{flow}\right) dt}{\int_0^{Tc} \left(U_c I_c + P_{flow}\right) dt} \tag{29}$$

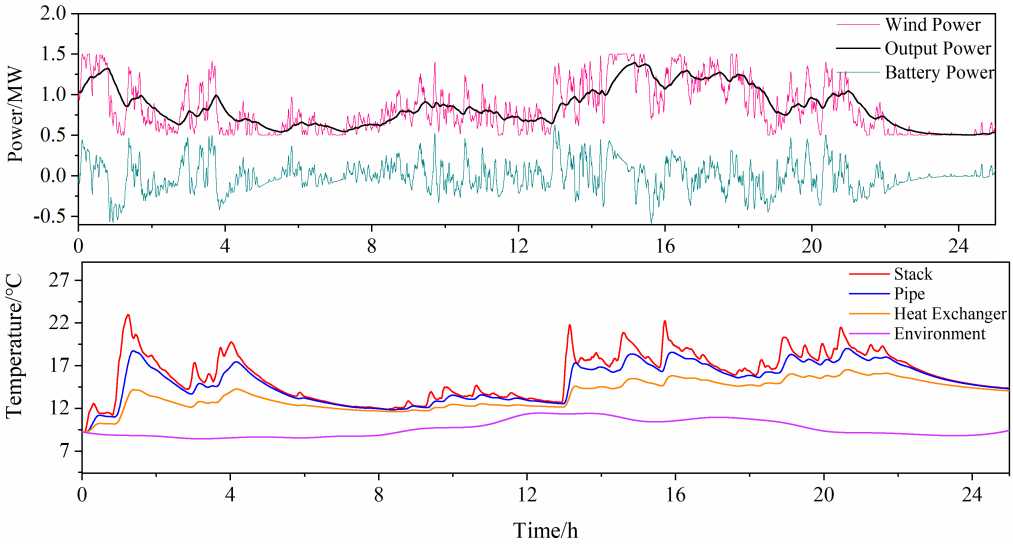

FIGURE 12. **Performance analysis for a Wind-VRB hybrid system. (a) Wind power smoothing using VRB. (b) Temperature variation during a typical day.**

where U_d and U_c are the discharge and charge voltage, T_d and T_c are the discharge and charge times, respectively. These efficiencies are utilized to evaluate the performance of the battery, and the efficiencies vs. current relationships are plotted in FIGURE 10 at different temperature levels. Note that the energy efficiency is defined as the ratio of the discharged energy to the charged energy in (27), while the system efficiency further incorporates the pump power loss in (28). The pump power is assumed to be constant since a constant flow rate is applied in this paper.

It can be observed from FIGURE 10(a) and (b) that as the applied current increases, the voltage efficiency reduces while the Coulomb efficiency increases. Furthermore, the trends of the voltage efficiency are opposite to that of the current efficiency. This is because a high charge current will cause a large amount of energy loss due to the internal overpotentials, and thus it can reduce the voltage efficiency. Meanwhile, the effect of self-discharge current reduces when the applied current increases, according to FIGURE 10(b).

In addition, high temperature increases voltage efficiency while it decreases the Coulomb efficiency. This is because under temperature condition, the properties of electrolytes and the permeability of the membrane can change dramatically. High temperature accelerates the chemical reaction rates of vanadium ions through the membrane and increases the conductivity of the electrolytes, resulting in a reduction of overpotentials. However, the high temperature will speed up the self-discharge process, which causes a decrease in Coulomb efficiency. Energy efficiency and system efficiency where are shown in FIGURE 10(c) and 10(d) respectively.

$$\mathbf{A} = \begin{bmatrix} -\frac{1}{R_{\text{act}}C_{\text{act}}} & 0 & 0 & 0 & 0 & 0 \\ 0 & -\frac{1}{R_{\text{con}}C_{\text{con}}} & 0 & 0 & 0 & 0 \\ 0 & 0 & 0 & 0 & 0 & 0 \\ 0 & 0 & 0 & -\frac{1}{R_{\text{th}-p}C_{\text{th}-s}} & \frac{1}{R_{\text{th}-p}C_{\text{th}-s}} & 0 \\ 0 & 0 & 0 & \frac{1}{R_{\text{th}-p}C_{\text{th}-p}} & -\frac{1}{R_{\text{th}-p}C_{\text{th}-p}} - \frac{1}{R_{\text{th-he}}C_{\text{th}-p}} & \frac{1}{R_{\text{th-he}}C_{\text{th}-p}} \\ 0 & 0 & 0 & 0 & \frac{1}{R_{\text{th-he}}C_{\text{th-he}}} & -\frac{1}{R_{\text{th-he}}C_{\text{th-he}}} - \frac{1}{R_{\text{th-air}}C_{\text{th-he}}} \end{bmatrix}$$

$$\mathbf{B} = \begin{bmatrix} \frac{1}{C_{\text{act}}} & \frac{1}{C_{\text{con}}} & -\frac{\eta}{C_n} & 0 & 0 & 0 \\ 0 & 0 & 0 & \frac{1}{C_{\text{th}-s}} & 0 & 0 \\ 0 & 0 & 0 & 0 & 0 & \frac{1}{R_{\text{th-air}}C_{\text{th-he}}} \end{bmatrix}^T$$

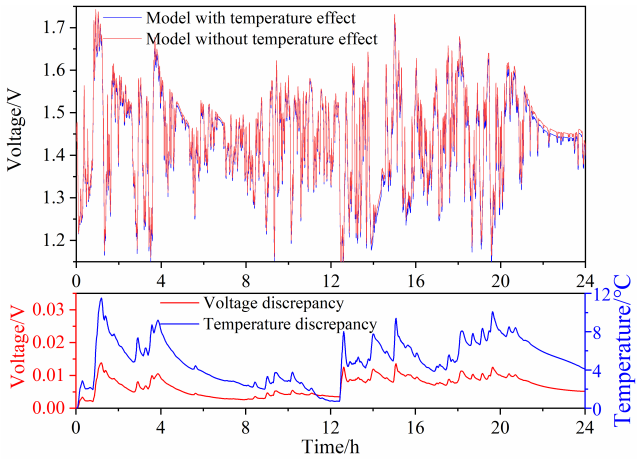

FIGURE 13. Voltage and temperature discrepancies between two models of VRB.

V. CASE STUDY

Battery energy storage systems can be used to smooth the power fluctuations and limit the ramp rate of the renewable generations [27]–[29]. In this section, a wind-VRB hybrid system is simulated and investigated to analyze the performance of the batteries. The wind power plant in conjunction with the VRB is connected to the utility grid via a back-to-back converter as shown in FIGURE 11. In this scenario, it is assumed that the ramp rate of the delivered power from the wind-VRB plant to the grid is limited in order to comply with the requirements of the grid code. The fluctuating wind power is thus smoothened using a low-pass filtering algorithm and the high-frequency components in the generated wind power are handled by the VRB.

The simulation was carried out based on the configuration of a 2MW direct-driven wind turbine generator and a 600kW/1200kWh VRB system. In addition, 24-hour real-world wind power data and measured ambient temperature were employed. The ambient temperature varies from 7 °C to 12 °C. The wind power, the output power with low-frequency components, and the VRB power with high-frequency components are shown in FIGURE 12(a). The predicted dynamic temperatures of the stack, the pipes, and the heat exchanger are shown in FIGURE 12(b). From FIGURE 12(b), a maximum difference of 13°C is observed between the stack electrolyte temperature and the ambient temperature. The peak stack temperature is reached in line with a drastic increase of the discharge power of the VRB. A great amount of heat is generated during the high discharge power period, and it causes the stack temperature to rise towards the upper limit. This shows the necessity to monitor the maximum power and to predict the stack temperature of the VRB so that measures can be taken to avoid the over-temperature problems. Furthermore, it can be seen that the electrolyte temperature in the stack is always higher than the temperatures in other components, since most of the heat is produced within the stack.

In order to evaluate the thermal effect, the comparison of voltage with and without considering temperature variation and its voltage temperature discrepancies are illustrated in FIGURE 13. A maximum of temperature discrepancy of 11.6 °C and a maximum of stack voltage discrepancy of 0.015 V per cell is observed.

VI. CONCLUSION

Conventional vanadium redox battery (VRB) models usually neglect the temperature effects on system performance. For a system-level design and operations of a grid-connected VRB system, an accurate mathematical model needs to be established to predict the system behaviors under various operating conditions. In this paper, an enhanced VRB model considering the coupled effects between the electrochemical and the thermal behaviors is proposed. The model consists of a second-order RC electrical circuit model and a third-order Cauer network. The Cauer network is utilized to describe the heat transfer process of stacks, the pipes and the heat exchangers. Furthermore, the parametric values of the developed model are identified using the particle swarm optimization (PSO) algorithm. The proposed model was then validated experimentally using a 5kW/3kWh VRB platform. The performance of a VRB system operated in conjunction with a wind power plant under practical conditions is investigated as a case study via simulation. The results show that the proposed coupled electro-thermal model can be employed to reflect the VRB performance under various operating conditions.

APPENDIX

The matrices **A** and **B** of the state-space model (18), as shown at the bottom of the previous page.

REFERENCES

[1] M. Skyllas-Kazacos, "Novel vanadium chloride/polyhalide redox flow battery," *J. Power Sources*, vol. 124, no. 1, pp. 299–302, 2003, doi: 10.1016/S0378-7753(03)00621-9.

[2] A. Trovò, G. Marini, A. Sutto, P. Alotto, M. Giomo, F. Moro, and M. Guarnieri, "Standby thermal model of a vanadium redox flow battery stack with crossover and shunt-current effects," *Appl. Energy*, vol. 240, pp. 893–906, Apr. 2019, doi: 10.1016/j.apenergy.2019.02.067.

[3] Y. Li, J. Bao, M. Skyllas-Kazacos, M. P. Akter, X. Zhang, and J. Fletcher, "Studies on dynamic responses and impedance of the vanadium redox flow battery," *Appl. Energy*, vol. 237, pp. 91–102, Mar. 2019, doi: 10.1016/j.apenergy.2019.01.015.

[4] P. Zhao, H. Zhang, H. Zhou, J. Chen, S. Gao, and B. Yi, "Characteristics and performance of 10 kW class all-vanadium redox-flow battery stack," *J. Power Sources*, vol. 162, no. 2, pp. 1416–1420, 2006, doi: 10.1016/j.jpowsour.2006.08.016.

[5] M. Skyllas-Kazacos and C. Menictas, "The vanadium redox battery for emergency back-up applications," in *Proc. Power Energy Syst. Converging Markets*, Melbourne, VIC, Australia, Oct. 1997, pp. 463–471, doi: 10.1109/INTLEC.1997.645928.

[6] X. Binyu, J. Zhao, W. Zhongbao, and Z. Chenda, "State of charge estimation of an all-vanadium redox flow battery based on a thermal-dependent model," in *Proc. IEEE PES Asia–Pacific Power Energy Eng. Conf. (APPEEC)*, Kowloon, China, Dec. 2013, pp. 1–6, doi: 10.1109/APPEEC.2013.6837290.

[7] X. Ma, H. Zhang, C. Sun, Y. Zou, and T. Zhang, "An optimal strategy of electrolyte flow rate for vanadium redox flow battery," *J. Power Sources*, vol. 203, pp. 153–158, Apr. 2012, doi: 10.1016/j.jpowsour.2011.11.036.

[8] A. Tang, S. Ting, J. Bao, and M. Skyllas-Kazacos, "Thermal modelling and simulation of the all-vanadium redox flow battery," *J. Power Sources*, vol. 203, pp. 165–176, Apr. 2012, doi: 10.1016/j.jpowsour.2011.11.079.

[9] B. Xiong, J. Zhao, K. J. Tseng, M. Skyllas-Kazacos, T. M. Lim, and Y. Zhang, "Thermal hydraulic behavior and efficiency analysis of an all-vanadium redox flow battery," *J. Power Sources*, vol. 242, pp. 314–324, Nov. 2013, doi: 10.1016/j.jpowsour.2013.05.092.

[10] B. Xiong, J. Zhao, Y. Su, Z. Wei, and M. Skyllas-Kazacos, "State of charge estimation of vanadium redox flow battery based on sliding mode observer and dynamic model including capacity fading factor," *IEEE Trans. Sustain. Energy*, vol. 8, no. 4, pp. 1658–1667, Oct. 2017, doi: 10.1109/TSTE.2017.2699288.

[11] F. Xing, H. Zhang, and X. Ma, "Shunt current loss of the vanadium redox flow battery," *J. Power Sources*, vol. 196, no. 24, pp. 10753–10757, 2011, doi: 10.1016/j.jpowsour.2011.08.033.

[12] Z. Wei, J. Zhao, M. Skyllas-Kazacos, and B. Xiong, "Dynamic thermal-hydraulic modeling and stack flow pattern analysis for all-vanadium redox flow battery," *J. Power Sources*, vol. 260, pp. 89–99, Aug. 2014, doi: 10.1016/j.jpowsour.2014.02.108.

[13] E. Agar, A. Benjamin, C. R. Dennison, D. Chen, M. A. Hickner, and E. C. Kumbur, "Reducing capacity fade in vanadium redox flow batteries by altering charging and discharging currents," *J. Power Sources*, vol. 246, pp. 767–774, Jan. 2014, doi: 10.1016/j.jpowsour.2013.08.023.

[14] R. D'Agostino, L. Baumann, A. Damiano, and E. Boggasch, "A Vanadium-redox-flow-battery model for evaluation of distributed storage implementation in residential energy systems," *IEEE Trans. Energy Convers.*, vol. 30, no. 2, pp. 421–430, Jan. 2015, doi: 10.1109/TEC.2014.2369437.

[15] X. Qiu, T. A. Nguyen, J. D. Guggenberger, M. L. Crow, and A. C. Elmore, "A field validated model of a vanadium redox flow battery for micro-grids," *IEEE Trans. Smart Grids*, vol. 5, no. 4, pp. 1592–1601, Jul. 2014, doi: 10.1109/TSG.2014.2310212.

[16] A. Tang, J. Bao, and M. Skyllas-Kazacos, "Dynamic modelling of the effects of ion diffusion and side reactions on the capacity loss for vanadium redox flow battery," *J. Power Sources*, vol. 196, no. 24, pp. 10737–10747, 2011, doi: 10.1016/j.jpowsour.2011.09.003.

[17] K. Wang, L. Liu, J. Xi, Z. Wu, and X. Qiu, "Reduction of capacity decay in vanadium flow batteries by an electrolyte-reflow method," *J. Power Sources*, vol. 338, pp. 17–25, Jan. 2017, doi: 10.1016/j.jpowsour.2016.11.031.

[18] Z. Wei, S. Meng, B. Xiong, D. Ji, and K. J. Tseng, "Enhanced online model identification and state of charge estimation for lithium-ion battery with a FBCRLS based observer," *Appl. Energy*, vol. 181, pp. 332–341, Nov. 2016, doi: 10.1016/j.apenergy.2016.08.103.

[19] Y. Li, M. Vilathgamuwa, S. S. Choi, T. W. Farrell, N. T. Tran, and J. Teague, "Development of a degradation-conscious physics-based lithium-ion battery model for use in power system planning studies," *Appl. Energy*, vol. 248, pp. 512–525, Aug. 2019, doi: 10.1016/j.apenergy.2019.04.143.

[20] Y. Li, M. Vilathgamuwa, T. Farrell, S. S. Choi, N. T. Tran, and J. Teague, "A physics-based distributed-parameter equivalent circuit model for lithium-ion batteries," *Electrochim. Acta*, vol. 299, pp. 451–469, Mar. 2019, doi: 10.1016/j.electacta.2018.12.167.

[21] Y. Zhang, J. Zhao, P. Wang, M. Skyllas-Kazacos, B. Xiong, and R. Badrinarayanan, "A comprehensive equivalent circuit model of all-vanadium redox flow battery for power system analysis," *J. Power Sour.*, vol. 290, pp. 14–24, Sep. 2015, doi: 10.1016/j.jpowsour.2015.04.169.

[22] B. Xiong, J. Zhao, Z. Wei, and M. Skyllas-Kazacos, "Extended Kalman filter method for state of charge estimation of vanadium redox flow battery using thermal-dependent electrical model," *J. Power Sources*, vol. 262, pp. 50–61, Sep. 2014, doi: 10.1016/j.jpowsour.2014.03.110.

[23] A. Tang, J. Bao, and M. Skyllas-Kazacos, "Studies on pressure losses and flow rate optimization in vanadium redox flow battery," *J. Power Sources*, vol. 248, pp. 154–162, Feb. 2014, doi: 10.1016/j.jpowsour.2013.09.071.

[24] Z. Abdmouleh, A. Gastli, L. Ben-Brahim, M. Haouari, and N. A. Al-Emadi, "Review of optimization techniques applied for the integration of distributed generation from renewable energy sources," *Renew. Energy*, vol. 113, pp. 266–280, Dec. 2017, doi: 10.1016/j.renene.2017.05.087.

[25] Z. Yu, L. Xiao, H. Li, X. Zhu, and R. Huai, "Model parameter identification for lithium batteries using the coevolutionary particle swarm optimization method," *IEEE Trans. Ind. Electron.*, vol. 64, no. 7, pp. 5690–5700, Jul. 2017, doi: 10.1109/TIE.2017.2677319.

[26] W. Xian, B. Long, M. Li, and H. Wang, "Prognostics of lithium-ion batteries based on the Verhulst model, particle swarm optimization and particle filter," *IEEE Trans. Instrum. Meas.*, vol. 63, no. 1, pp. 2–17, Jan. 2014, doi: 10.1109/TIM.2013.2276473.

[27] J. Fang, Q. Zeng, X. Ai, Z. Chen, and J. Wen, "Dynamic optimal energy flow in the integrated natural gas and electrical power systems," *IEEE Trans. Sustain. Energy*, vol. 9, no. 1, pp. 188–198, Jan. 2018, doi: 10.1109/TSTE.2017.2717600.

[28] J. Liu, J. Wen, W. Yao, and Y. Long, "Solution to short-term frequency response of wind farms by using energy storage systems," *IET Renew. Power Gener.*, vol. 10, no. 5, pp. 669–678, May 2016, doi: 10.1049/iet-rpg.2015.0164.

[29] H. Shuai, J. Fang, X. Ai, J. Wen, and H. He, "Optimal real-time operation strategy for microgrid: An ADP-based stochastic nonlinear optimization approach," *IEEE Trans. Sustain. Energy*, vol. 10, no. 2, pp. 931–942, Apr. 2019, doi: 10.1109/TSTE.2018.2855039.

BINYU XIONG (S'11–M'16) received the B.E. degree in electrical engineering from Wuhan University, Wuhan, China, in 2010, and the M.Sc. and Ph.D. degrees from the Nanyang Technological University, Singapore, in 2011 and 2016, respectively.

He is currently an Associate Professor with the School of Automation, Wuhan University of Technology, Wuhan. His research interests include electrical and thermal modeling of batteries, battery state of charge estimation, large-scale energy storage systems, power electronics, and renewable energy generations.

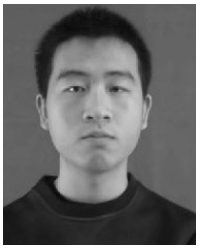

YESEN YANG is currently pursuing the bachelor's degree with the School of Automation, Wuhan University of Technology, Wuhan, China. His major is electrical engineering and automation. His research interests include energy storage systems, electrical and thermal modeling of batteries, power electronics, and renewable energy generations.

JINRUI TANG (M'16) received the B.S. degree in electrical engineering from Zhejiang University, Hangzhou, China, in 2009, and the Ph.D. degree in electrical engineering from the School of Electrical and Electronic Engineering, Huazhong University of Science and Technology, Wuhan, China, in 2014.

He is currently an Associate Professor with the School of Automation, Wuhan University of Technology. His research interests include distribution network protection and automation, planning and analysis of hybrid AC/DC power systems with distributed generation.

YANG LI (S'11–M'16) received the B.E. degree in electrical engineering from Wuhan University, Wuhan, China, in 2007, and the M.Sc. and Ph.D. degrees in power engineering from Nanyang Technological University (NTU), Singapore, in 2008 and 2015, respectively.

From 2015 to 2016, he was a Research Fellow at the Energy Research Institute at NTU (ERI@N), Singapore. From 2016 to 2018, he was a Research Fellow at the School of Electrical Engineering and Computer Science, Queensland University of Technology, Brisbane, Australia. He joined the School of Automation, Wuhan University of Technology, Wuhan, in 2019, where he is currently an Associate Professor. His research interests include modeling and control of lithium-ion batteries, renewable generation, and applications of battery energy storage in power systems and transport sectors.

ZHONGBAO WEI received the B.Eng. degree, in 2010, the M.Sc. degree from Beihang University, China, in 2013, and the Ph.D. degree from Nanyang Technological University, Singapore, in 2017. He has been a Research Fellow at the Energy Research Institute @ NTU, Nanyang Technological University, from 2016 to 2018. He is currently a Professor with the National Engineering Laboratory for Electric Vehicles, School of Mechanical Engineering, Beijing Institute of Technology, China. He has authored more than 30 peer-reviewed articles. His research interests include battery modeling, identification, state estimation, diagnostic, and thermal management, with applications to renewable energy systems such as lithium-ion battery and vanadium redox flow battery.

YIXIN SU received the M.S. degree in control theory and application from the Institute of Automation, Southeast University, Nanjing, China, in 1988, and the Ph.D. degree in mechanical manufacturing and automation from the Huazhong University of Science and Technology, Wuhan, China, in 2006. He is currently a Professor with the School of Automation, Wuhan University of Technology, Wuhan, China. His current research interests include intelligent control, system optimization, and marine motion control.

QINGYONG ZHANG received the M.S. degree in applied control science and engineering from the Wuhan University of Technology, Wuhan, China, in 2009. She is currently a Senior Experimenter and Doctoral Student with the School of Automation, Wuhan University of Technology, Wuhan. Her current research interests include intelligent system optimization, and control and production scheduling.